# Topological charge-density method of identifying phase singularities in cardiac fibrillation

Yin-Jie He,[1] Qi-Hao Li,[1] Kuangshi Zhou,[2] Ruhong Jiang,[2] Chenyang Jiang,[2] Jun-Ting Pan,[3] Dafang Zheng,[1] Bo Zheng,[4,1,*] and Hong Zhang[1,†]

[1]*Zhejiang Institute of Modern Physics and Department of Physics, Zhejiang University, Hangzhou 310027, China*
[2]*Department of Cardiology, Sir Run Run Shaw Hospital, School of Medicine, Zhejiang University, Hangzhou 310016, China*
[3]*Ocean College, Zhejiang University, Zhoushan 316021, China*
[4]*School of Physics and Astronomy, Yunnan University, Kunming 650091, China*

(Received 15 March 2021; accepted 28 June 2021; published 20 July 2021)

Spiral waves represent the key motifs of typical self-sustained dynamical patterns in excitable systems such as cardiac tissue. The motion of phase singularities (PSs) that lies at the center of spiral waves captures many qualitative and, in some cases, quantitative features of their complex dynamics. Recent clinical studies suggested that ablating the tissue at PS locations may cure atrial fibrillation. Here, we propose a different method to determine the location of PSs. Starting from the definition of the topological charge of spiral waves, we obtain the expression of the topological charge density in a discrete case. With this expression, we can calculate the topological charge at each grid in the space directly, so as to accurately identify the position of PSs.

DOI: 10.1103/PhysRevE.104.014213

## I. INTRODUCTION

Excitable media, such as cardiac tissue and some chemical media, can support a large amplitude excitation wave under a superthreshold stimulus. Following the wave, there is a refractory period during which a new excitation cannot be induced. Spiral waves in excitable media have great effects on diverse physical, chemical, and biological systems [1–3]. In cardiology, such self-sustained waves play an essential role in tachycardia and fibrillation [4,5].

Spiral waves can be stationary, meandering, or even degenerate into multiple unstable rotating waves. The spatiotemporal behavior of spiral waves has been extensively quantified by tracking the trajectory of their phase singularities (PSs), i.e., the core of spiral waves. The analysis of PS dynamics is thus important for exploring the mechanisms of cardiac fibrillation [6]. Recently, clinical studies have suggested that ablating the tissue at PS locations may cure fibrillation of the cardiac atria [7].

For numerical simulations, locating the intersection point of the isocontours of the two-state variables is a classic method to determine the position of the PS [8–10]. Though robust and suitable for numerical simulations, the two-state variables needed in this method are not experimentally accessible. Only one dependent variable (generally voltage $V$) is usually recorded in experiment. Therefore, how to use one variable to detect the PS has aroused widespread concern.

In this paper, a charge-density method of identifying PSs using only one variable is proposed. First, according to the definition of the topological charge of spiral waves, we derive the expression of the topological charge density in a discrete case. Then, using the discrete expression of the topological charge density, we directly and accurately calculate the topological charge at each grid in two-dimensional system space: the topological charge at PSs will be $+1$ or $-1$ while others are 0, which helps us distinguish the PSs clearly. We illustrate the principle of this method and give its comparison with the convolution method [11,12].

## II. METHODS

### A. Model simulations

First, we consider the classic two-variable FitzHugh-Nagumo (FHN) model [13,14] described with the following equations:

$$\frac{\partial V}{\partial t} = \frac{1}{\varepsilon}\left(V - \frac{V^3}{3} - W\right) + D\nabla^2 V, \tag{1a}$$

$$\frac{\partial W}{\partial t} = \varepsilon(V + \beta - \gamma W), \tag{1b}$$

where $V$ is the fast (voltage) variable while $W$ is the slow (gating) variable; $D$ is the diffusion coefficient; $\varepsilon$, $\beta$, and $\gamma$ are model parameters. In this paper, we set $D = 1.00$, $\varepsilon = 0.22$, $\beta = 0.70$, and $\gamma = 0.80$. The whole simulation based on Eq. (1) is running in a $512 \times 512$ array with no-flux boundary conditions, whose spatial discretization $\Delta x = \Delta y = 0.05$ and temporal discretization $\Delta t = 0.0005$. Note that, in clinical usage, such high spatial resolution can't be achieved. Therefore, in order to improve the authenticity of simulation, we take a sample every four grids, which means we only obtain a spiral wave in the range of $128 \times 128$ grids with $Lx = Ly = 25.6$, as illustrated in Fig. 1(a). Figure 1(a) is a snapshot which describes the spatial distribution of the fast variable $V$ of a meandering spiral wave generated by the FHN model.

*Corresponding author: zhengbo@zju.edu.cn
†Corresponding author: hongzhang@zju.edu.cn

 

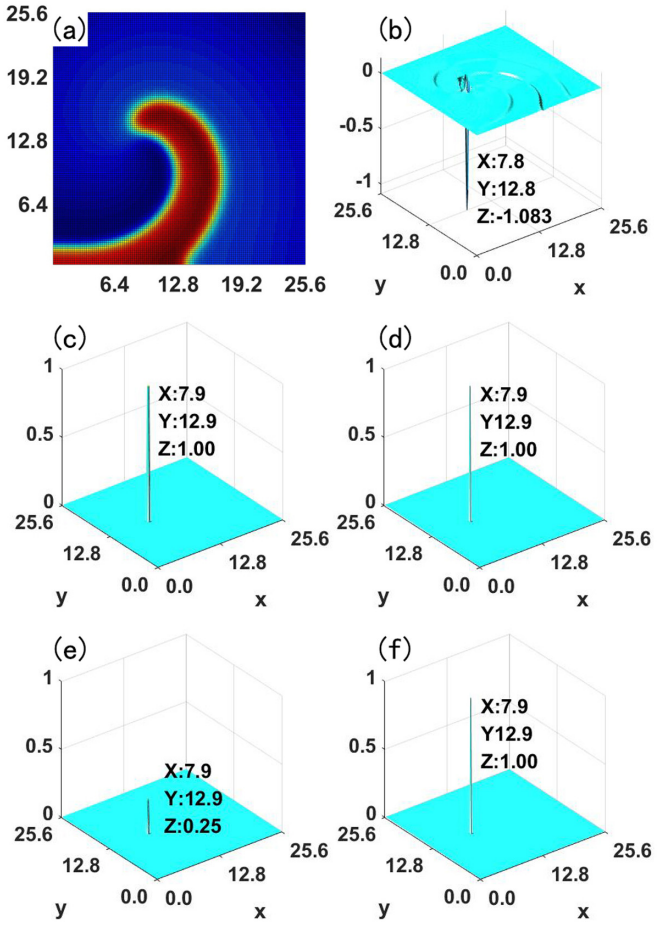


FIG. 1. FHN model was used to simulate spiral waves with $\varepsilon = 0.22$, $\beta = 0.70$, and $\gamma = 0.80$. (a) The spatial distribution of the fast variable $V$ of a meandering spiral wave. Panels (b)–(f) show the distribution of the topological charge $\rho(i, j)\Delta x^2$ in two-dimensional space. The coordinates of PSs identified by different methods are marked in these figures respectively. (b) Convolution method with Sobel $3 \times 3$ convolutional kernels. (c) Convolution method with nabla $3 \times 3$ convolutional kernels. (d) Convolution method with nabla $2 \times 2$ convolutional kernels. (e) Charge-density method with $3 \times 3$ arrays. (f) Charge-density method with $2 \times 2$ arrays.

### B. Phase mapping

Phase mapping is a technique to assess the complexity of the dynamics. This approach is applicable to numerical simulations, optical mapping experiments as well as electrical recordings. The phase at each point represents the state of each moment, so it is significant to obtain the actual phase mapping. PSs are points where all values of the phase converge and correspond to the core of spiral waves. Experimentally, one can calculate the phase with only one state variable (generally voltage $V$) by using a reconstructed state space [15], which is formed by $V(t)$ and $V(t+\tau)$. The pseudo-EMD (PEMD) [16] is an effective way to detrend the fast variable $V$, and we will use it to process the data before calculating the phase.

First of all, we construct the envelope of the maximum and the minimum of $V(t)$, marked $V_{\max}(t)$ and $V_{\min}(t)$, respectively. The envelope midline $V_{\text{mean}}(t)$ then is computed by

$$V_{\text{mean}}(x, y, t) = \frac{V_{\max}(x, y, t) + V_{\min}(x, y, t)}{2}. \tag{2}$$

We finally detrend $V(t)$ by computing

$$V'(x, y, t) = V(x, y, t) - V_{\text{mean}}(x, y, t). \tag{3}$$

By the same operation on $V(t + \tau)$, we obtain

$$V'(x, y, t + \tau) = V(x, y, t + \tau) - V_{\text{mean}}(x, y, t + \tau) \tag{4}$$

as well. The expression of the phase for each grid using $V'(t + \tau)$ and $V'(t)$ is

$$\phi(x, y, t) = \arctan 2[V'(x, y, t + \tau), V'(x, y, t)], \tag{5}$$

where the function $\arctan 2$ will return a value of the phase within $(-\pi, +\pi]$. We will use Eq. (5) in the following calculation and set the time delay $\tau$ as $0.2T$ ($T$ is the period of the spiral wave).

### C. Charge-density method

The neighboring elements of PSs exhibit a continuous progression of the phase which is equal to $\pm 2\pi$ around them [15]. This is described in terms of the topological charge [17–19] defined as

$$n_t = \frac{1}{2\pi} \oint_\Gamma \vec{k} \cdot d\vec{l}, \quad \vec{k} = \nabla\phi, \tag{6}$$

where $\Gamma$ represents a closed curve surrounding the PS. Whether the line integral is $+2\pi$ or $-2\pi$, i.e., $n_t = +1$ or $n_t = -1$, depends on the chirality of the spiral [20]. Specifically, using Stokes' theorem, we transform Eq. (6) into

$$n_t = \frac{1}{2\pi} \iint_S (\nabla \times \vec{k}) \cdot \hat{z} d\sigma, \tag{7}$$

where the surface $S$ is surrounded by $\Gamma$ in Eq. (6). Thus, the charge density can be expressed as

$$\rho(x, y) = \frac{1}{2\pi} (\nabla \times \vec{k}) \cdot \hat{z}. \tag{8}$$

In the meantime, according to the topological current theory [21,22], it is rigorously proven that [23]

$$\rho(x, y) = \delta[V'(t + \tau)]\delta[V'(t)]D^0(V'/x), \tag{9}$$

where $D^0(V'/x) = \partial_x V'(t)\partial_y V'(t + \tau) - \partial_y V'(t)\partial_x V'(t + \tau)$ is the Jacobian determinant and $\delta$ is the Dirac delta function.

As shown in Ref. [23], we know that

$$\rho(x, y) = n_t \delta(x - x_{ps})\delta(y - y_{ps}). \tag{10}$$

Under the condition of discrete data,

$$\delta(x - x_{ps})\delta(y - y_{ps}) \to \delta_{i,i^*}\delta_{j,j^*}/\Delta x^2,$$

which means that Eq. (8) can be rewritten as

$$\rho(i, j) = \frac{1}{2\pi}[(\nabla \times \vec{k}) \cdot \hat{z}]_{i,j} = n_t \delta_{i,i^*}\delta_{j,j^*}/\Delta x^2. \tag{11}$$

Thus,

$$\rho(i,j)\Delta x^2 = \frac{1}{2\pi}[(\nabla \times \vec{k})\cdot\hat{z}]_{i,j}\Delta x^2 = n_t \delta_{i,i^*}\delta_{j,j^*}, \quad (12)$$

where $\rho(i,j)\Delta x^2$ represents the topological charge within the area of $\Delta x^2$ centered on $(i,j)$. Using Eq. (12), we can calculate $\rho(i,j)\Delta x^2$ at each grid. According to the above theoretical analysis, if the grid is a PS, i.e., $(i^*, j^*)$, the value of $\rho(i,j)\Delta x^2$ will be $+1$ or $-1$. Otherwise, the value of $\rho(i,j)\Delta x^2$ is 0.

When we use the charge-density method for numerical simulation, it is performed as follows: The gradient of the phase is defined by a finite difference operation in the $x$ and $y$ directions:

$$\frac{\partial\phi}{\partial x}\left(i+\frac{1}{2},j+\frac{1}{2}\right) = \frac{\phi\left(i+1,j+\frac{1}{2}\right)-\phi\left(i,j+\frac{1}{2}\right)}{\Delta x}, \quad (13a)$$

$$\frac{\partial\phi}{\partial y}\left(i+\frac{1}{2},j+\frac{1}{2}\right) = \frac{\phi\left(i+\frac{1}{2},j+1\right)-\phi\left(i+\frac{1}{2},j\right)}{\Delta x}. \quad (13b)$$

After that,

$$\frac{\partial^2\phi}{\partial y\partial x}\left(i+\frac{1}{2},j+\frac{1}{2}\right) = \frac{\frac{\partial\phi}{\partial y}\left(i+1,j+\frac{1}{2}\right)-\frac{\partial\phi}{\partial y}\left(i,j+\frac{1}{2}\right)}{\Delta x}, \quad (14a)$$

$$\frac{\partial^2\phi}{\partial x\partial y}\left(i+\frac{1}{2},j+\frac{1}{2}\right) = \frac{\frac{\partial\phi}{\partial x}\left(i+\frac{1}{2},j+1\right)-\frac{\partial\phi}{\partial x}\left(i+\frac{1}{2},j\right)}{\Delta x}, \quad (14b)$$

and

$$[(\nabla \times \vec{k})\cdot\hat{z}]_{i+\frac{1}{2},j+\frac{1}{2}} = \frac{\partial^2\phi}{\partial y\partial x}\left(i+\frac{1}{2},j+\frac{1}{2}\right) - \frac{\partial^2\phi}{\partial x\partial y}\left(i+\frac{1}{2},j+\frac{1}{2}\right),$$

so, we rewrite Eq. (12) as

$$\rho\left(i+\frac{1}{2},j+\frac{1}{2}\right)\Delta x^2 = \frac{1}{2\pi}\left[\frac{\partial^2\phi}{\partial y\partial x}\left(i+\frac{1}{2},j+\frac{1}{2}\right) - \frac{\partial^2\phi}{\partial x\partial y}\left(i+\frac{1}{2},j+\frac{1}{2}\right)\right]\Delta x^2. \quad (15)$$

It should be ensured that the value of the phase change between two grids is within the range $(-\pi, +\pi]$ [24].

If we want to calculate $\rho(i+\frac{1}{2}, j+\frac{1}{2})\Delta x^2$, we need the phase nearby $(i+\frac{1}{2}, j+\frac{1}{2})$ in the range of $2\times 2$ arrays. Figure 1(f) is obtained by the charge-density method with $2\times 2$ arrays and the result is straightforward: in the field of $\rho(i+\frac{1}{2}, j+\frac{1}{2})\Delta x^2$, there is only one peak equal to $+1$ and others are 0, which is consistent with the above derivation. So we can clearly identify the location of the PS and mark its coordinate in the picture.

We can also expand the range from $2\times 2$ to $3\times 3$ arrays if we define the gradient of the phase in this way:

$$\frac{\partial\phi}{\partial x}(i,j) = \frac{[\phi(i+1,j)-\phi(i,j)]+[\phi(i,j)-\phi(i-1,j)]}{2\Delta x}, \quad (16a)$$

$$\frac{\partial\phi}{\partial y}(i,j) = \frac{[\phi(i,j+1)-\phi(i,j)]+[\phi(i,j)-\phi(i,j-1)]}{2\Delta x}, \quad (16b)$$

where the value of the phase change between two adjacent grids is within the range $(-\pi, +\pi]$ and

$$\frac{\partial^2\phi}{\partial y\partial x}(i,j) = \frac{\frac{\partial\phi}{\partial y}(i+1,j)-\frac{\partial\phi}{\partial y}(i-1,j)}{2\Delta x}, \quad (17a)$$

$$\frac{\partial^2\phi}{\partial x\partial y}(i,j) = \frac{\frac{\partial\phi}{\partial x}(i,j+1)-\frac{\partial\phi}{\partial x}(i,j-1)}{2\Delta x}. \quad (17b)$$

Therefore,

$$\rho(i,j)\Delta x^2 = \frac{1}{2\pi}\left[\frac{\partial^2\phi}{\partial y\partial x}(i,j) - \frac{\partial^2\phi}{\partial x\partial y}(i,j)\right]\Delta x^2. \quad (18)$$

The result obtained by $3\times 3$ arrays [see Fig. 1(e)] is slightly different from that of $2\times 2$ arrays [see Fig. 1(f)]: there are four peaks equal to $+0.25$ and others are 0. It can be explained as follows: When we use the phase nearby $(i,j)$ in the range of $3\times 3$ arrays, Eq. (11) should be rewritten as

$$\rho(i,j) = \frac{1}{2\pi}[(\nabla \times \vec{k})\cdot\hat{z}]_{i,j} = n_t\delta_{i,i^*}\delta_{j,j^*}/(2\Delta x)^2,$$

that is,

$$\rho(i,j)\Delta x^2 = \tfrac{1}{4}n_t\delta_{i,i^*}\delta_{j,j^*}.$$

Thus, the peak value is indeed $+0.25$ and there are four peaks equal to $+0.25$. This makes sure that the surface integral of Eq. (7) is equal to $+1$. In other words, the charge-density method with $3\times 3$ arrays identifies four points with $\rho(i,j)\Delta x^2 = 0.25$ and the PS is located in the center of these

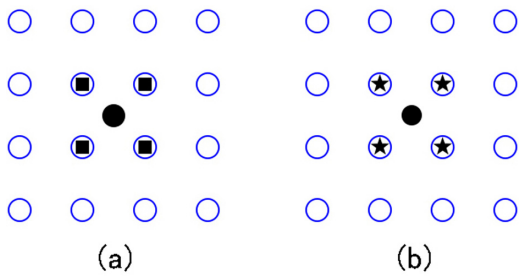


FIG. 2. Simple schematics are used to illustrate the charge-density method and the convolution method. (a) Using charge-density method with $3 \times 3$ arrays obtains four points marked by black squares with $\rho(i, j)\Delta x^2 = 0.25$. The center of these four points is identified as a PS (black dot). (b) Using convolution method with nabla $3 \times 3$ convolutional kernels identifies four PSs which are marked by black stars and the real PS (black dot) is located in the intersection of these PSs.

points, as shown in Fig. 2(a). So we mark the coordinate of the center point in Fig. 1(e) as the position of the PS.

### D. Convolution method

For comparison, we use the convolution method developed by Bray *et al.* [11,12] to identify the location of a PS, which has been widely used since proposed [25–29]. They proposed that the line integral of Eq. (6) can be expressed as a convolution operation:

$$(\nabla \times \vec{k}) \cdot \hat{z} \equiv \lim_{S\to 0} \frac{1}{S} \oint_{\Gamma} \vec{k} \cdot d\vec{l} \propto (\nabla_x \otimes k_y + \nabla_y \otimes k_x)/\Delta x. \tag{19}$$

Combining Eq. (19) with Eq. (11), we get

$$\rho(i, j) = \frac{1}{2\pi}(\nabla_x \otimes k_y + \nabla_y \otimes k_x)/\Delta x,$$

that is,

$$\rho(i, j)\Delta x^2 = \frac{1}{2\pi}(\nabla_x \otimes k_y + \nabla_y \otimes k_x)\Delta x, \tag{20}$$

where $k_x$ and $k_y$ are $\frac{\partial \phi}{\partial x}$ and $\frac{\partial \phi}{\partial y}$, respectively; $\otimes$ is convolution operation, and

$$\nabla_x = \begin{bmatrix} -1/2 & 0 & 1/2 \\ -1 & 0 & 1 \\ -1/2 & 0 & 1/2 \end{bmatrix}, \quad \nabla_y = \begin{bmatrix} 1/2 & 1 & 1/2 \\ 0 & 0 & 0 \\ -1/2 & -1 & -1/2 \end{bmatrix} \tag{21}$$

are Sobel $3 \times 3$ convolutional kernels [11].

The value of the convolution operation Eq. (20) should be $\pm 1$ and its sign depends on the chirality of the rotation. However, the value of Eq. (20) with Sobel $3 \times 3$ convolution kernels not only is not strictly $\pm 1$ at a PS, but also is not equal to 0 at other points, as shown in Fig. 1(b). Therefore, we think Sobel $3 \times 3$ convolution kernels are not suitable for determining PSs.

Actually, Sobel $3 \times 3$ kernels were first used in image edge detection, not PS detection. And later, Bray changed the kernels used in the convolution method, named nabla kernels [12], which are derivative operators similar to Prewitt operators used in image processing [30] and which are appropriate for evaluating the differential form of the curl operation. Therefore, in this paper, we will use the following two kinds of convolution kernels to locate PSs, the result of which will be compared with that of the charge-density method:

nabla $3 \times 3$ kernels [12],

$$\nabla_x = \begin{bmatrix} 1 & 0 & -1 \\ 1 & 0 & -1 \\ 0 & 0 & 0 \end{bmatrix}, \quad \nabla_y = \begin{bmatrix} -1 & -1 & 0 \\ 0 & 0 & 0 \\ 1 & 1 & 0 \end{bmatrix}, \tag{22}$$

and nabla $2 \times 2$ kernels [12],

$$\nabla_x = \begin{bmatrix} 1 & -1 \\ 0 & 0 \end{bmatrix}, \quad \nabla_y = \begin{bmatrix} -1 & 0 \\ 1 & 0 \end{bmatrix}. \tag{23}$$

Figures 1(c) and 1(d) illustrate the results performed by the convolution method with nabla $3 \times 3$ kernels and nabla $2 \times 2$ kernels, respectively. We know from Fig. 1(c) that the convolution method with nabla $3 \times 3$ kernels identifies four PSs close together. But the real PS is located in the intersection of these PSs, as shown in Fig. 2(b). We mark the coordinate of the intersection of these PSs in Fig. 1(c) as the position of the real PS. In line with expectations, the convolution method with nabla $2 \times 2$ kernels only obtains one point whose $n_t$ is $+1$ while other points are 0, so we distinguish the PS point clearly [see Fig. 1(d)].

## III. RESULTS

### A. PS trajectory

After the theoretical analysis, here is a comparison of the charge-density method and the convolution method. We record the PS trajectories obtained by four different methods, including the convolution method with nabla $3 \times 3$ kernels, the convolution method with nabla $2 \times 2$ kernels, the charge-density method with $3 \times 3$ arrays, and the charge-density method with $2 \times 2$ arrays. We don't use the convolution method with Sobel $3 \times 3$ kernels due to its imperfect result as shown in Fig. 1(b). All the PS trajectories are generated with the FHN model with the same parameters as those in Fig. 1 and PS points are recorded once per time unit. The results show that all these trajectories obtained by the four methods are exactly the same as each other, which reveals the fact that these four methods have the same performance in this case (see Fig. 3).

### B. Noise

In practice, there are many factors that affect the accuracy of data. Among all the factors, the influence of noise [24,31] can't be ignored. In order to study the effect of noise, the FHN model's parameters are the same as those in Fig. 1 while we add spatiotemporal white noise $\sigma(x, y, t)$ [31] to the right side of Eq. (1a), in which $\langle \sigma(x, y, t) \rangle = 0$, $\langle \sigma(x, y, t)\sigma(x', y', t') \rangle = \eta\delta(x-x')\delta(y-y')\delta(t-t')$.

We set the value of the noise amplitude as 0.004, i.e., $\eta = 0.004$. The influence of noise on the spiral wave is seen in Fig. 4(a). Because of noise, the result of the convolution method with Sobel $3 \times 3$ kernels [Fig. 4(b)] gets even worse. Nevertheless, the convolution method with nabla $3 \times 3$

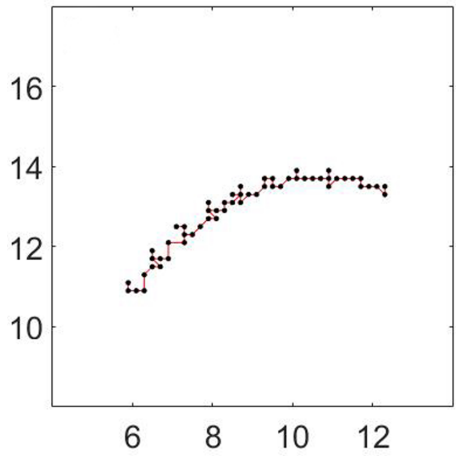


FIG. 3. One of the four identical trajectories obtained by four different methods. PS points are recorded once per time unit from 140 to 260 time units. All these four methods lead to the exactly same trajectories, and for brevity, it just shows the trajectory obtained by the charge-density method with $3 \times 3$ arrays.

kernels, the convolution method with nabla $2 \times 2$ kernels, the charge-density method with $3 \times 3$ arrays, and the charge-density method with $2 \times 2$ arrays, as shown in Figs. 4(c)–4(f), respectively, still identify the PSs accurately. It is further found that the PS trajectories obtained by these four methods are strictly identical when under the same amplitude, which means that these four methods have the same performance under the same noise amplitude. Taking the trajectories obtained by the charge-density method with $3 \times 3$ arrays as an example, Fig. 5 illustrates the variation of trajectories under different noise amplitudes. When the noise is weak, e.g., $\eta = 0.0002$, the overall PS trajectory of the spiral wave is roughly the same as that in the case of no noise as shown in Fig. 3, but there are differences in details [see Fig. 5(a)]. With the increase of noise amplitudes, the overall PS trajectory changes gradually. When the noise is strong enough, e.g., $\eta = 0.004$, the PS trajectory changes significantly with the direction of the motion obviously shifted.

Meanwhile, we also take the PS-detecting error rate as the standard to judge whether the method is good enough. First, we have to define the PS-detecting error rate [25,32]: the number of false results (false-positive plus false-negative PSs) divided by the total number of recording times. When the PS is not detected at the position where it actually exists, or when the number of the PSs detected exceeds their actual numbers, we regard such results as false results. For the methods with $3 \times 3$ arrays, when the four grids around the PS are not close together as shown in Fig. 2, it is also regarded as false results. At the same time, we take the PS position obtained by manual verification as the "gold standard" to ensure the detection of the PS properly, as mentioned in Refs. [25,29].

According to this definition, we obtain the error rate of different methods in the process of tracking PSs. As shown in Table I, the error rate of the charge-density method and the convolution method increases with the increase of the noise amplitude, but their performance is identical under the same noise amplitude.

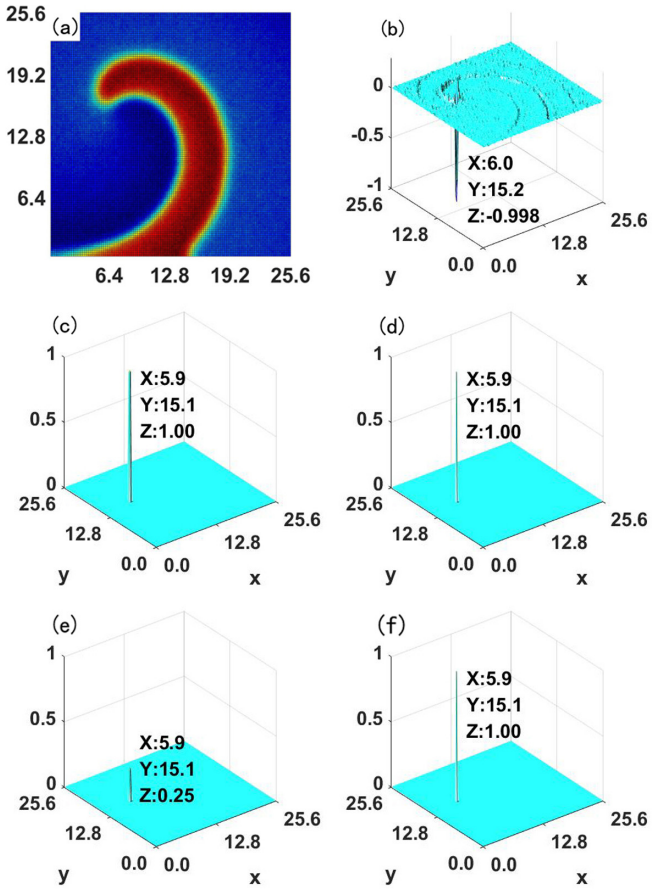


FIG. 4. The effect of noise. The FHN model's parameters are the same as those in Fig. 1 while the noise amplitude $\eta = 0.004$. (a) The spatial distribution of the fast variable $V$ of a meandering spiral wave. Panels (b)–(f) show the distribution of the topological charge $\rho(i, j)\Delta x^2$ in two-dimensional space. The coordinates of PSs identified by different methods are marked in these figures respectively. (b) Convolution method with Sobel $3 \times 3$ convolutional kernels. (c) Convolution method with nabla $3 \times 3$ convolutional kernels. (d) Convolution method with nabla $2 \times 2$ convolutional kernels. (e) Charge-density method with $3 \times 3$ arrays. (f) Charge-density method with $2 \times 2$ arrays.

### C. Multiple PSs

Sometimes there are multiple spiral waves observed in the heart during fibrillation, so it is significant to test the charge-density method's ability to locate PSs of multiple spiral waves. We carry out the simulation on a larger system consisting of $1024 \times 1024$ grids with spatial discretization $\Delta x = \Delta y = 0.05$ and temporal discretization $\Delta t = 0.0005$, i.e., $Lx = Ly = 51.2$. And we still take a simple every four grids and finally, we just obtain multiple spiral waves in the range of $256 \times 256$ grids with $Lx = Ly = 51.2$, as shown in Fig. 6(a). In this case, the convolution method with Sobel $3 \times 3$ kernels is still not suitable for identifying the PSs, whose result is not accurate enough [see Fig. 6(b)]. All the other methods [see Figs. 6(c)–6(f)] not only identify the location of PSs perfectly, but also figure out the rotation direction of spiral waves. Thus, the charge-density method is an effective way to identify PSs in the case of multiple spiral waves.

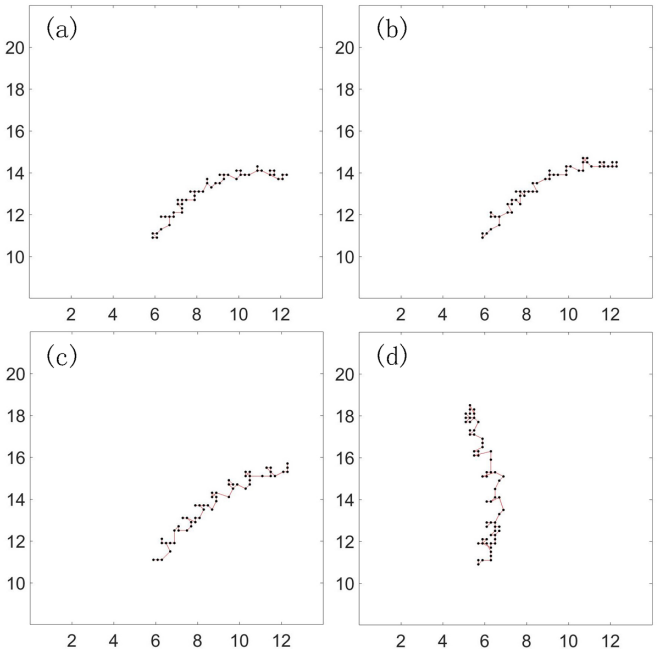


FIG. 5. PS trajectories obtained by the charge-density method with 3 × 3 arrays under different noise amplitudes. The initial conditions are the same as those in Fig. 3. PS points are recorded once per time unit and the time duration is the same as that in Fig. 3. (a) $\eta = 0.0002$. (b) $\eta = 0.0005$. (c) $\eta = 0.001$. (d) $\eta = 0.004$.

### D. Spatial resolution

Electric and optical mapping are two well-known methods that are commonly used for acquiring electrograms during fibrillation [33]. Even though a relatively high spatial resolution is obtained with optical mapping, it cannot be used in human heart due to the toxicity of the fluorescent dyes. Electric mapping has no such limitation and in electric mapping experiments, the surface of the heart (epi and/or endo) will be covered with electrode array to record the activity of the heart for each sampling instant of the acquisition. However, the number of electrodes is not enough to collect all the details on the surface of the heart, which means that we only get low spatial resolution data.

If we want to know whether the charge-density method is available at low spatial resolution, we have to further reduce the spatial resolution to 32 × 32, as shown in Fig. 7(a), which just records 0.39% of the data from the real system (512 × 512). Figures 7(b)–7(f) show the results from different methods. Again the convolution method with Sobel 3 × 3 kernels [Fig. 7(b)] is not suitable. The charge-density method with 3 × 3 arrays and 2 × 2 arrays identify the PS with the coordinate (8.4, 13.2), as well as the convolution method with nabla 3 × 3 kernels and nabla 2 × 2 kernels. We record the PS trajectories obtained by these four different methods at this spatial resolution and find that all the trajectories are exactly the same. As shown in Fig. 8, the trend of the trajectory is similar to that in Fig. 3.

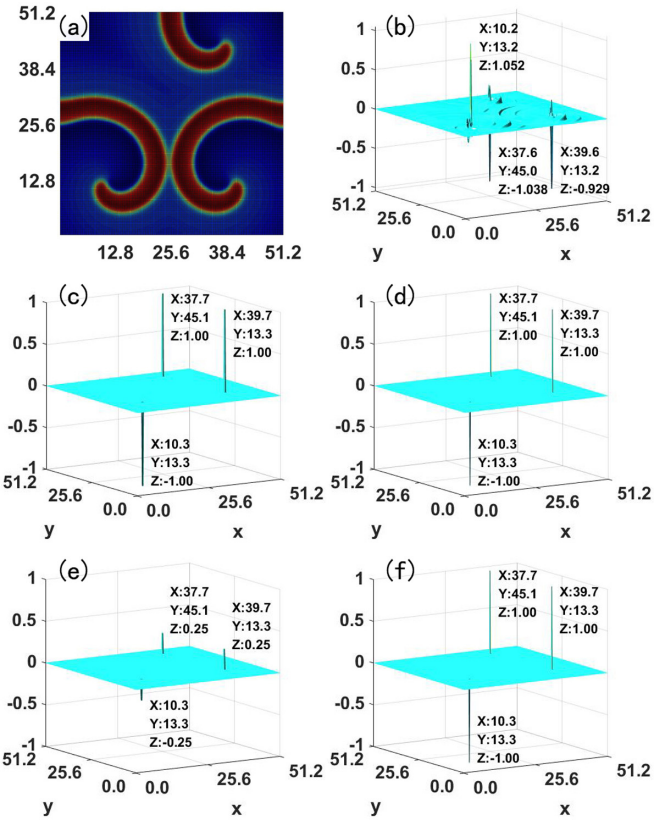


FIG. 6. Use different methods to identify PSs for multiple spiral waves. The simulation, in the range of 256 × 256 grids, used the same model and parameters as those in Fig. 1. (a) The spatial distribution of the fast variable $V$ of multiple spiral waves. Panels (b)–(f) show the distribution of the topological charge $\rho(i, j)\Delta x^2$ in two-dimensional space. The coordinates of PSs identified by different methods are marked in these figures respectively. (b) Convolution method with Sobel 3 × 3 convolutional kernels. (c) Convolution method with nabla 3 × 3 convolutional kernels. (d) Convolution method with nabla 2 × 2 convolutional kernels. (e) Charge-density method with 3 × 3 arrays. (f) Charge-density method with 2 × 2 arrays.

At the same time, in order to better understand the performance of various methods in low spatial resolution, we investigate the PS-detecting error rates under the 32 × 32

TABLE I. PS-detecting error rates caused by noise.

| | Convolution method nabla 3 × 3 | Convolution Method nabla 2 × 2 | Charge-density method 3 × 3 arrays | Charge-density method 2 × 2 arrays |
|---|---|---|---|---|
| $\eta = 0.0002$ | 0.00% | 0.00% | 0.00% | 0.00% |
| $\eta = 0.0005$ | 1.67% | 1.67% | 1.67% | 1.67% |
| $\eta = 0.001$ | 2.50% | 2.50% | 2.50% | 2.50% |
| $\eta = 0.004$ | 5.00% | 5.00% | 5.00% | 5.00% |

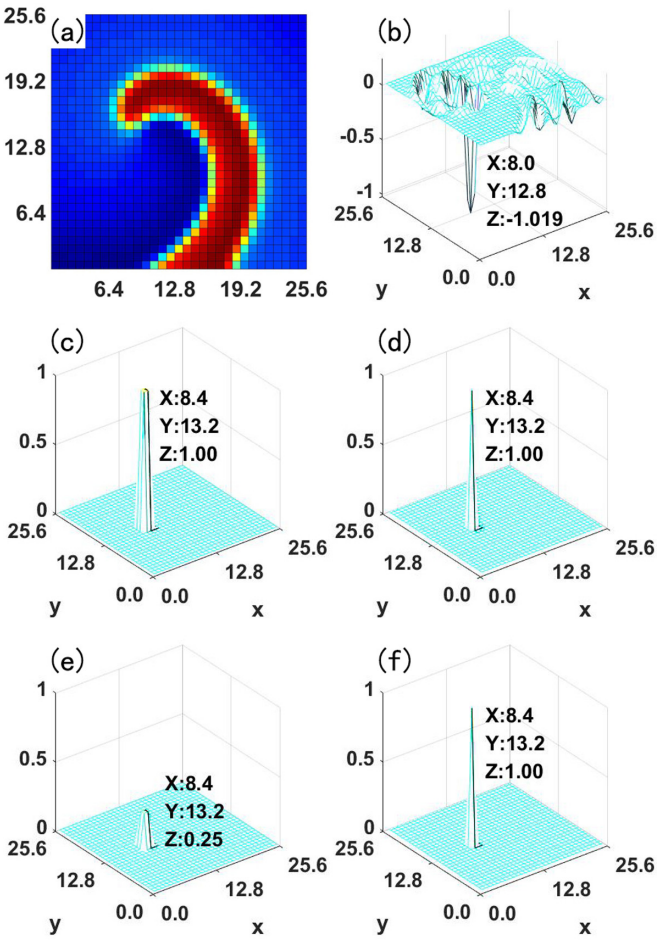


FIG. 7. The effect of spatial resolution. The FHN model's parameters are the same as those in Fig. 1 while the spatial resolution reduced from $128 \times 128$ to $32 \times 32$. (a) The spatial distribution of the fast variable $V$ of a meandering spiral wave. Panels (b)–(f) show the distribution of the topological charge $\rho(i, j)\Delta x^2$ in two-dimensional space. The coordinates of PSs identified by different methods are marked in these figures respectively. (b) Convolution method with Sobel $3 \times 3$ convolutional kernels. (c) Convolution method with nabla $3 \times 3$ convolutional kernels. (d) Convolution method with nabla $2 \times 2$ convolutional kernels. (e) Charge-density method with $3 \times 3$ arrays. (f) Charge-density method with $2 \times 2$ arrays.

spatial resolution as shown in Table II. All these four methods work well with 0% error rates. Note that only $8 \times 8$ electrodes are available in clinical usage currently [7], so we also calculate the PS-detecting error rates under the $8 \times 8$ spatial resolution in Table II, which shows that the charge-density method has the error rate of 2.5% as well as the convolution method.

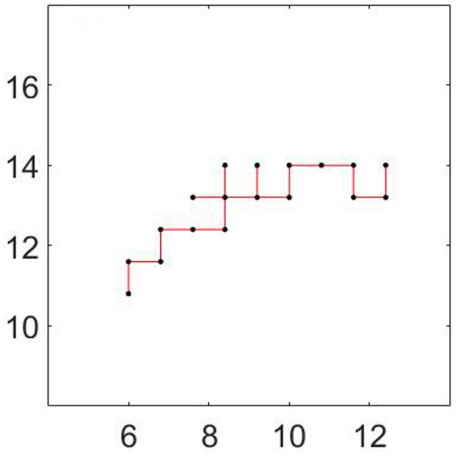

FIG. 8. One of the four identical trajectories obtained by four different methods with low spatial resolution ($32 \times 32$). PS points are recorded once per time unit and the time duration is the same as that in Fig. 3. All these four methods lead to the exactly same trajectories, and for brevity, it just shows the trajectory obtained by the charge-density method with $3 \times 3$ arrays.

### E. Luo-Rudy model

Aiming to apply the charge-density method to cardiac data, we use the Luo-Rudy model [34] to simulate spiral waves in the heart, which is described with the following equation:

$$\frac{\partial V}{\partial t} = -\frac{I_{\text{ion}}}{C_m} + \nabla \cdot (D \nabla V), \tag{24}$$

where $V$ is the transmembrane potential. $C_m = 1\ \mu\text{F/cm}^2$ is the membrane capacitance and $D = 0.001\ \text{cm}^2/\text{ms}$ is the diffusion constant. $I_{\text{ion}}$ is the total ionic current density of the membrane and all the parameters refer to Ref. [35]. Equation (24) is integrated using the Euler method with spatial discretization $\Delta x = \Delta y = 0.0075$ cm and temporal discretization $\Delta t = 0.00125$ ms. The whole simulation is running in a $512 \times 512$ array with no-flux boundary conditions. Then we take a sample every eight grids to obtain a spiral wave in $64 \times 64$ arrays with $Lx = Ly = 3.84$ cm, as illustrated in Fig. 9(a). The result of the convolution method with Sobel $3 \times 3$ kernels [Fig. 9(b)] is not satisfactory while the convolution method with nabla $3 \times 3$ kernels [Fig. 9(c)] and nabla $2 \times 2$ kernels [Fig. 9(d)] identify the PS accurately. Note that the charge-density method with $3 \times 3$ arrays in Fig. 9(e) still locates four points with an average $n_t$ of 0.25 and the center of these points is the PS. The charge-density method with $2 \times 2$ arrays in Fig. 9(f) identifies the PS directly. From Figs. 9(e) and 9(f), we know that the charge-density method works well when applied to cardiac data.

TABLE II. PS-detecting error rates for different spatial resolution.

| | Convolution method nabla $3 \times 3$ | Convolution method nabla $2 \times 2$ | Charge-density method $3 \times 3$ arrays | Charge-density method $2 \times 2$ arrays |
|---|---|---|---|---|
| $32 \times 32$ | 0 | 0 | 0 | 0 |
| $8 \times 8$ | 2.5% | 2.5% | 2.5% | 2.5% |

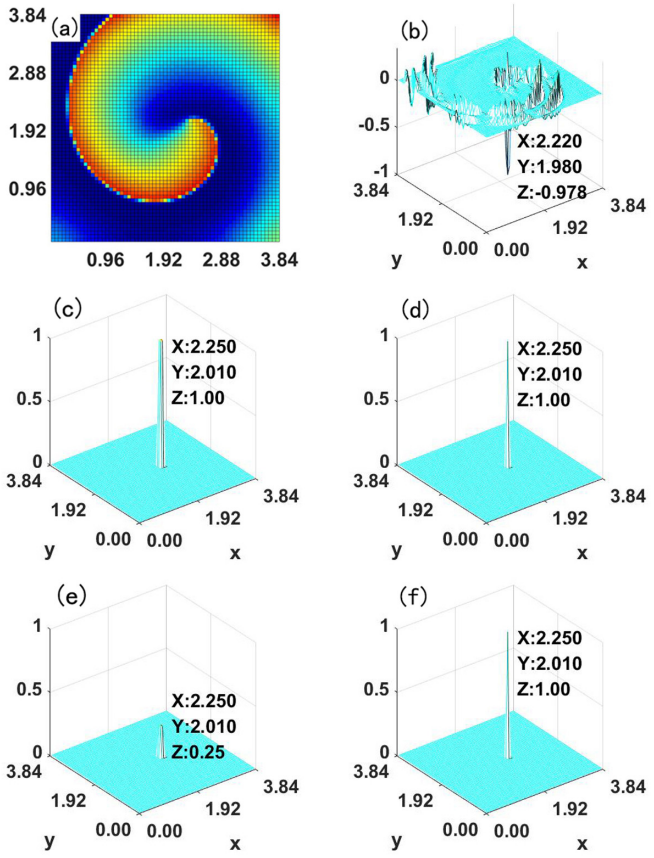


FIG. 9. Luo-Rudy model was used to simulate spiral waves in cardiac tissues. All parameters are chosen the same as those in Fig. 3A(a) in Ref. [35]. (a) The spatial distribution of a spiral wave in cardiac tissues (64 × 64). Panels (b)–(f) show the distribution of the topological charge $\rho(i, j)\Delta x^2$ in two-dimensional space. The coordinates of PSs identified by different methods are marked in these figures respectively. (b) Convolution method with Sobel 3 × 3 convolutional kernels. (c) Convolution method with nabla 3 × 3 convolutional kernels. (d) Convolution method with nabla 2 × 2 convolutional kernels. (e) Charge-density method with 3 × 3 arrays. (f) Charge-density method with 2 × 2 arrays.

PS trajectories of spiral waves generated with the Luo-Rudy model are obtained by four different methods, including the convolution method with nabla 3 × 3 kernels, the convolution method with nabla 2 × 2 kernels, the charge-density method with 3 × 3 arrays, and the charge-density method with 2 × 2 arrays. All of these four methods get the same patterns. Namely, the PSs recorded during a long time series give rise to a flowerlike pattern with outward petals (see Fig. 10).

We also calculate the PS-detecting error rates of four different methods in the case of coarser resolution. Table III

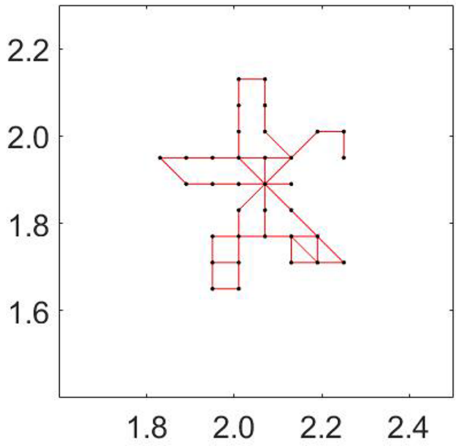


FIG. 10. One of the four identical trajectories obtained by four different methods with Luo-Rudy model. All these four methods lead to the exactly same trajectories, and for simplicity, it just shows the trajectory obtained by the charge-density method with 3 × 3 arrays.

illustrates the error rates of different methods under the 32 × 32 and the 8 × 8 spatial resolution. No matter what the spatial resolution is, the performance of these four methods is identical. Note that, when the spatial resolution reduces from 32 × 32 to 8 × 8, the error rate increases from 0.0% to 8.0%.

## IV. DISCUSSION AND CONCLUSION

From the previous discussions and comparisons, we find that the charge-density method and the convolution method have the same good performance when they are applied to detecting PSs in different situations. Nevertheless, the charge-density method and the convolution method have the following differences: (1) The charge-density method in Eq. (12) is strictly derived in theory and the algorithm used in numerical simulation is unique; however, the convolution method in Eq. (20) has neither a strict derivation nor a unique algorithm, whose results depend on the convolution kernels: nabla kernels are effective for identifying PSs while Sobel kernels are not suitable. (2) The charge-density method, compared with the convolution method, is easier to understand and calculate.

In conclusion, we have developed a different approach for identifying the locations of PSs. Based on the topological current theory and the definition of the topological charge of spiral waves, we derive the expression of the topological charge density in a discrete case. According to this discrete expression, we can not only directly and accurately calculate the topological charge at each grid in the two-dimensional system space, but also theoretically obtain that the topological

TABLE III. PS-detecting error rates for different spatial resolution.

| | Convolution method nabla 3 × 3 | Convolution method nabla 2 × 2 | Charge-density method 3 × 3 arrays | Charge-density method 2 × 2 arrays |
|---|---|---|---|---|
| 32 × 32 | 0 | 0 | 0 | 0 |
| 8 × 8 | 8.0% | 8.0% | 8.0% | 8.0% |

charge at PSs will be $+1$ or $-1$ while others are 0. With the charge-density method, we can locate the position of PSs accurately by simple calculations. In order to illustrate the robustness of the charge-density method, we further apply this method to the cases of noise, low spatial resolution, multiple spiral waves, and the Luo-Rudy model, and it turns out that the charge-density method is effective in all of these cases.

**ACKNOWLEDGMENTS**

We are grateful to M.-A. Bray for kindly providing the code of the convolution method used in this paper for comparison, and to K.-Q. Yang, Y.-L. Zhang, and T.-C. Li for valuable discussions. This work was supported by the National Natural Science Foundation of China under Grants No. 12075203 and No. 11775186.

[1] A. T. Winfree, *The Geometry of Biological Time* (Springer, New York, 2001).
[2] Z. Qu, G. Hu, A. Garfinkel, and J. N. Weiss, Phys. Rep. **543**, 61 (2014).
[3] S. Alonso, M. Bär, and B. Echebarria, Rep. Prog. Phys. **79**, 096601 (2016).
[4] J. M. Davidenko, A. V. Pertsov, R. Salomonsz, W. Baxter, and J. Jalife, Nature (London) **355**, 349 (1992).
[5] S. M. Narayan, D. E. Krummen, and W.-J. Rappel, J. Cardiovasc. Electrophysiol. **23**, 447 (2012).
[6] S. Nattel, F. Xiong, and M. Aguilar, Nat. Rev. Cardiol. **14**, 509 (2017).
[7] S. M. Narayan, D. E. Krummen, K. Shivkumar, P. Clopton, W.-J. Rappel, and J. M. Miller, J. Am. Coll. Cardiol. **60**, 628 (2012).
[8] A. T. Winfree, *When Time Breaks Down* (Princeton University Press, Princeton, NJ, 1987).
[9] A. T. Winfree, Chaos **1**, 303 (1991).
[10] D. Barkley, M. Kness, and L. S. Tuckerman, Phys. Rev. A **42**, 2489 (1990).
[11] M.-A. Bray, S.-F. Lin, R. R. Aliev, B. J. Roth, and J. P. Wikswo, Jr., J. Cardiovasc. Electrophysiol. **12**, 716 (2001).
[12] M.-A. Bray and J. P. Wikswo, IEEE Trans. Biomed. Eng. **49**, 1086 (2002).
[13] R. FitzHugh, Biophys. J. **1**, 445 (1961).
[14] J. Nagumo, S. Arimoto, and S. Yoshizawa, Proc, IRE **50**, 2061 (1962).
[15] R. A. Gray, A. M. Pertsov, and J. Jalife, Nature (London) **392**, 75 (1998).
[16] M.-A. Bray and J. P. Wikswo, Phys. Rev. E **65**, 051902 (2002).
[17] N. D. Mermin, Rev. Mod. Phys. **51**, 591 (1979).
[18] A. Goryachev and R. Kapral, Phys. Rev. Lett. **76**, 1619 (1996).
[19] J. Davidsen, L. Glass, and R. Kapral, Phys. Rev. E **70**, 056203 (2004).
[20] J.-T. Pan, M.-C. Cai, B.-W. Li, and H. Zhang, Phys. Rev. E **87**, 062907 (2013).
[21] Y. S. Duan and M. L. Ge, Sci. Sin. **11**, 1072 (1979).
[22] Y. S. Duan and H. Zhang, Phys. Rev. E **60**, 2568 (1999).
[23] D.-B. Pan, B.-W. Li, J.-T. Pan, Q.-H. Li, and H. Zhang, New J. Phys. **22**, 103015 (2020).
[24] A. N. Iyer and R. A. Gray, Ann. Biomed. Eng. **29**, 47 (2001).
[25] R. Zou, J. Kneller, L. J. Leon, and S. Nattel, Chaos **12**, 764 (2002).
[26] M. Valderrabano, P. S. Chen, and S. F. Lin, Circulation **108**, 354 (2003).
[27] C. P. Bradley, R. H. Clayton, M. P. Nash, A. Mourad, M. Hayward, D. J. Paterson, and P. Taggart, Circ.: Arrhythmia Electrophysiol. **4**, 684 (2011).
[28] C. H. Roney, C. D. Cantwell, J. D. Bayer, N. A. Qureshi, P. B. Lim, J. H. Tweedy, P. Kanagaratnam, N. S. Peters, E. J. Vigmond, and F. Siong, Circ.: Arrhythmia Electrophysiol. **10**, e004899 (2017).
[29] X. Li, T. P. Almelda, N. Dastagir, M. S. Guillem, J. Salinet, G. S. Chu, P. J. Stafford, F. S. Schlindwein, and G. A. Ng, Front. Physiol. **11**, 869 (2020).
[30] R. C. Gonzales and R. E. Woods, *Digital Image Processing* (Pearson Education, Inc., Upper Saddle River, NJ, 2008).
[31] J. Garcia-Ojalvo and J. M. Sancho, *Noise in Spatially Extended Systems* (Springer, New York, 1999).
[32] T.-C. Li, D.-B. Pan, K. Zhou, R. Jiang, C. Jiang, B. Zheng, and H. Zhang, Phys. Rev. E **98**, 062405 (2018).
[33] K. Umapathy, K. Nair, S. Masse, S. Krishnan, J. Rogers, M. P. Nash, and K. Nanthakumar, Circ.: Arrhythmia Electrophysiol. **3**, 105 (2010).
[34] C. H. Luo and Y. Rudy, Circ. Res. **68**, 1501 (1991).
[35] Z. Qu, F. Xie, A. Garfinkel, and J. N. Weiss, Ann. Biomed. Eng. **28**, 755 (2000).